Hybridizable Discontinuous Galerkin p-adaptivity for wave propagation problems

Giorgio Giorgiani, Sonia Fernández-Méndez and Antonio Huerta*

Laboratori de Calcul Numeric (LaCaN). Departament de Matematica Aplicada III
E.T.S. de Ingenieros de Caminos, Canales y Puertos,
Universitat Politecnica de Catalunya – BarcelonaTech, Jordi Girona 1, 08034 Barcelona, Spain.
web http://www.lacan.upc.edu

SUMMARY

A p-adaptive Hybridizable Discontinuous Galerkin method for the solution of wave problems is presented in a challenging engineering problem. Moreover, its performance is compared with a high-order continuous Galerkin. The hybridization technique allows to reduce the coupled degrees of freedom to only those on the mesh element boundaries, while the particular choice of the numerical fluxes opens the path to a super-convergent post-processed solution. This super-convergent post-processed solution is used to construct a simple and inexpensive error estimator. The error estimator is employed to obtain solutions with the prescribed accuracy in the area (or areas) of interest and also drives a proposed iterative mesh adaptation procedure. The proposed method is applied to a non-homogeneous scattering problem in an unbounded domain. This is a challenging problem because, on one hand, for high frequencies numerical difficulties are an important issue due to the loss of the ellipticity and the oscillatory behavior of the solution. And on the other hand, it is applied to real harbor agitation problems. That is, the Mild Slope equation in frequency domain (Helmholtz equation with non-constant coefficients) is solved on real geometries with the corresponding perfectly matched layer to damp the diffracted waves. The performance of the method is studied on two practical examples. The adaptive Hybridizable Discontinuous Galerkin method exhibits better efficiency compared to a high-order continuous Galerkin method using static condensation of the interior nodes.

Received ...

KEY WORDS: Scattering, Helmholtz equation, discontinuous Galerkin method, p-adaptivity, error estimation, high-order approximations, hybridization.

*Correspondence to: A. Huerta, Laboratori de Càlcul Numèric (LaCàN), E.T.S. Ingenieros de Caminos, Universitat Politècnica de Catalunya, Jordi Girona 1, E-08034 Barcelona, Spain.

Contract/grant sponsor: Ministerio de Educación y Ciencia & Generalitat de Catalunya AGAUR; contract/grant number: DPI2011-27778-C02-02 & 2009SGR875

1. INTRODUCTION

Wave propagation is a challenging problem present in many engineering applications. Acoustic waves, electromagnetism and vibrations are examples of physical phenomena that are modeled with wave equations. The assumption of a harmonic solution leads to Helmholtz-type wave equations, with non-constant coefficients in the general case. Solving this problem for high frequencies leads to numerical difficulties because of the loss of the elliptic character and the oscillatory behavior of the solution. The key issue is the control of the so-called pollution effect, associated mainly with the dispersive nature of the numerical waves. Many techniques have been proposed in the past to reduce the pollution effect. Stabilized finite elements [1, 2, 3, 4, 5] is probably the most popular. Embedding the oscillatory behavior of the solution in the approximating functions is another option to improve accuracy, see for instance [6, 7, 8, 9, 10, 11, 12].

An interesting application of wave propagation in an inhomogeneous media is the refraction/diffraction of sea waves over an uneven bottom in an unbounded domain. The so-called Mild Slope equation (MSE) is a widely used model to simulate the propagation of sea waves from the open sea to the interior of the harbor. Due to the importance of the MSE in engineering, various numerical models have been proposed, among those, finite differences [13, 14], finite and infinite elements [15, 16], finite elements coupled with boundary elements [17]. Nevertheless, in engineering practice, the usual approach is standard low-order finite elements, namely, continuous Galerkin (CG) with a piecewise linear or quadratic approximation [18, 19].

Recent results [20, 21, 22, 23, 24, 25] reveal that high-order computations can be more efficient than low-order ones. In fact, [23] indicates that high-order elements, in this case $p \geq 2$, provide better accuracy for same number of degrees of freedom (DOF), or require less computational cost for a desired accuracy level, even for engineering purpose. Obviously, adjusting locally the polynomial order of interpolation to the needs of a smooth solution, enables exploiting the advantages of high-order elements. However, p-adaptive computations in the context of CG have had little success because they need special FE, such as FE with blending functions [26, 27], or mortar elements [28], to impose C^0 continuity of the approximation, leading to a cumbersome implementation.

On the contrary, discontinuous Galerkin methods (DG) [29, 30, 31] provide a natural framework for p-variable FE computations: an element by element discontinuous approximation is considered and required continuity is weakly imposed through numerical fluxes.

DG methods are always hampered, compared to CG, by their larger number of DOF. Nevertheless, recent contributions in wave propagation problems show more efficient DG computations compared with their CG counterpart. They are restricted, however, to low-order approaches. For instance, in [32], the interior penalty discontinuous Galerkin performs better than CG in the pre-asymptotic range (large element size) for the Helmholtz equation. In [33], a discontinuous finite element formulation of the Helmholtz equation is proposed, which also requires less DOF than CG for properly chosen parameters. However, both [32] and [33] do not exploit high-order approximations, they use linear functional approximations and compare the results with a standard CG (that is, a non-stabilized approach). A comparison with, for instance, a GLS stabilized approach [2] would have been more fair.

Note that for an honest comparison between CG and DG, CG should be implemented exploiting the uncoupling of local (interior) DOF between elements. Until very recently, DG methods coupled

interior nodes with neighboring element nodes, even for reduced stencil approaches such as interior penalty methods [34, 30] and Compact Discontinuous Galerkin method (CDG) [31]. Under these circumstances, as will be shown in the examples, the number of DOF for CDG is always larger than CG for a given precision. Recently, however, a novel DG approach has been proposed where every interior node is uncoupled from neighboring element nodes: the hybridizable discontinuous Galerkin method (HDG), see for example [35, 36, 37, 38]. The similarity between hybridization in DG and static condensation in CG is highlighted in [39]. For non-adaptive computations in an academic wave equation example, HDG performs similarly to CG, providing almost identical accuracy for a similar computational cost, see [39].

Furthermore, the particular flux choice in HDG provides an optimal converging approximation not only for the solution but also for its gradient. Then, an element-by-element post-processing technique induces a super-convergent approximation. This characteristic, unique of the HDG method, is a major advantage for adaptive techniques: the post-process provides a reference solution that can be used for error estimation purposes. The error estimator induced by the HDG post-process proves to be reliable with a marginal computational cost. Here a p-adaptive HDG method with error estimation induced by the local post-process is proposed for the solution of the MSE.

The paper is organized as follows. Section 2 presents the problem statement for the MSE with a Perfectly Matched Layer (PML) to model non-reflecting boundaries [40, 41]. The p-variable HDG method for the MSE is recalled in Section 3. Section 4 is devoted to the error estimation and the p-adaptive algorithm. Numerical examples in Section 5 demonstrate the applicability and good performance of the proposed p-adaptive HDG method for problems of engineering interest such as wave propagation in harbors.

2. PROBLEM STATEMENT: THE MILD SLOPE EQUATION WITH PML

The MSE is a 2D Helmholtz equation with non-constant coefficients. Derived by Berkhoff in 1972 [42], the MSE describes the propagation of sea waves over a slow varying bathymetry, in shallow and deep water, for bottom slopes up to 1/3 [43]. The linearity of the model and its range of applicability make it a valuable tool for harbor agitation studies. Moreover, with the inclusion of additional terms, it is possible to take into account non-linear effects such as bottom friction [44] and wave breaking [45].

The MSE is derived after integrating along the vertical axis the 3D incompressible Navier-Stokes equations with the assumption of inviscid fluid, small amplitude waves and slow varying bottom. In frequency formulation, it is written as

$$\boldsymbol{\nabla}\cdot\left(cc_g\nabla\hat{\eta}\right)+k^2cc_g\hat{\eta}=0, \tag{1}$$

where $\hat{\eta}(x,y)\in\mathbb{C}$ is the surface elevation function, $k(x,y)\in\mathbb{R}$ is the wave number, $c(x,y)\in\mathbb{R}$ is the phase wave velocity, $c_g=d\omega/dk\in\mathbb{R}$ is the group wave velocity, and $\omega\in\mathbb{R}$ is the angular frequency assumed to be constant in the whole domain in the MSE model, see [42] for more details. The wave number $k(x,y)$ is coupled with the depth function $h(x,y)$ by means of the non-linear

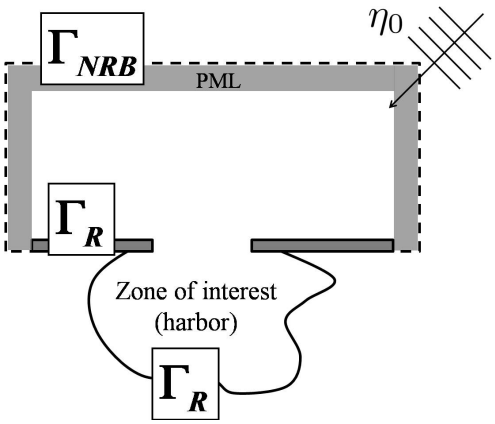

Figure 1. Computational domain with PML

dispersion relation

$$\omega^2 = kg\tanh(kh),$$

being g the gravity acceleration. Reflecting and absorbing boundaries Γ_{R}, such as beaches, dikes or breakwaters, are modeled by Robin-type boundary conditions

$$\nabla\hat{\eta}\cdot\boldsymbol{n} = ik\alpha\hat{\eta} \quad \text{on } \Gamma_{\mathrm{R}},$$

where $\boldsymbol{n}$ is the unitary outward normal at the boundary, i is the imaginary unit and $\alpha \in [0,1]$ is a real coefficient. It is equal to zero on totally reflecting walls and to one on totally absorbing boundaries, see for instance [46].

An artificial boundary Γ_{NRB} is considered to define the bounded computational domain Ω in $\mathbb{R}^2$, see Figure 1. A PML is used to avoid reflections from outgoing waves, see for instance [40] for a general presentation. A constant bottom depth is set in the PML region to obtain a non-reflecting media. The problem to be solved is then

$$\boldsymbol{\nabla\cdot}\left(cc_g\mathbf{P}\nabla\eta\right) + k^2 s_x s_y cc_g\eta = -s_x s_y B(\eta_0), \qquad \text{in } \Omega, \tag{2a}$$

$$\nabla\eta\cdot\boldsymbol{n} - ik\alpha\eta = -(\nabla\eta_0\cdot\boldsymbol{n} - ik\alpha\eta_0), \qquad \text{on } \Gamma_{\mathrm{R}}, \tag{2b}$$

$$\mathbf{P}\nabla\eta\cdot\boldsymbol{n} - ik\eta = 0, \qquad \text{on } \Gamma_{\mathrm{NRB}}. \tag{2c}$$

where η denotes the reflected wave and $\eta_0 = \exp\left(ik_0\boldsymbol{d_0}\cdot\boldsymbol{x}\right)$, with $\boldsymbol{x} = \{x, y\}$, is the incident wave, characterized by the wave number k_0 and its direction $\boldsymbol{d_0} = (\cos\theta_0, \sin\theta_0)$. The total wave is then $\hat{\eta} = \eta + \eta_0$. Matrix $\mathbf{P}$ in (2a) is the anisotropy matrix defining the absorption in the PML medium. Obviously, $\mathbf{P} = \mathbf{I}$ outside the PML. The operator defined by the Berkhoff equation, see (1), is denoted by $B(\cdot)$ and it is applied to the incident potential. The absorption parameters in the two Cartesian directions are s_x and s_y. Equation (2c) is a first order absorbing condition imposed on the PML exterior boundary to minimize wave reflections.

3. HYBRIDIZABLE DISCONTINUOUS GALERKIN FOR THE MSE

The domain Ω is partitioned in a set of $\mathtt{n_{el}}$ disjoint elements, $\mathcal{T}_h = \{K_j : j = 1, \ldots, \mathtt{n_{el}}\}$ with boundaries ∂K_j defining the set of element boundaries $\partial\mathcal{T}_h = \{\partial K : K \in \mathcal{T}_h\}$. For two neighboring elements K^+ and K^- of the collection $\mathcal{T}_h$, $\partial K^+ \cap \partial K^-$ is the interior side between K^+ and K^-, and for elements K along the boundary, $\partial K \cap \partial\Omega$ is the boundary side. The set of interior sides is $\mathcal{E}_h^i$, while the global set of interior and boundary sides is denoted as $\mathcal{E}_h$. Edges are generically denoted by F, i.e. $F \in \mathcal{E}_h$.

The following finite element spaces $\boldsymbol{V}_h(\mathcal{T}_h)$, $P_h(\mathcal{T}_h)$ and $M_h(\mathcal{E}_h)$ associated to $\mathcal{T}_h$ and to $\mathcal{E}_h$ are also introduced

$$
\begin{aligned}
\boldsymbol{V}_h &:= \left\{\boldsymbol{v} \in [L^2(\Omega)]^2 : \boldsymbol{v}|_K \in [\mathcal{P}^{p_K}(K)]^2, \forall K \in \mathcal{T}_h\right\},\\
P_h &:= \left\{q \in L^2(\Omega) : q|_K \in \mathcal{P}^{p_K}(K), \forall K \in \mathcal{T}_h\right\},\\
M_h &:= \left\{\mu \in L^2(\mathcal{E}_h) : \mu|_F \in \mathcal{P}^{p_F}(F), \forall F \in \mathcal{E}_h\right\},
\end{aligned}
$$

where $\mathcal{P}^p$ denotes the space of polynomials of degree $\leq p$, while p_K and p_F are the polynomial degrees in element K and side F respectively.

Remark 1
In general, the polynomial degree for elements, and sides, can vary from element to element, and from side to side. More precisely, in all computations, given a map of elemental degrees, the interpolation degree p_F for a side shared by two elements, $F = \partial K^+ \cap \partial K^-$, is set as the maximum value of the degree in K^+ and K^-, that is $p_F = \max\{p_{K^+}, p_{K^-}\}$, and $p_F = p_K$ when $F \in \partial K \cap \partial\Omega$. This procedure ensures a well posed problem and the superconvergent properties of the method, see [38].

The following standard scalar products are also defined

$$
\left(\boldsymbol{v}, \boldsymbol{\omega}\right)_K = \int_K \boldsymbol{v} \cdot \boldsymbol{\omega}\, d\Omega, \quad \left(p, q\right)_K = \int_K pq\, d\Omega, \quad \text{and} \quad \left\langle p, q\right\rangle_{\partial K} = \int_{\partial K} pq\, d\Gamma.
$$

The HDG formulation is deduced from the first order system equivalent to (2a) over the "broken" computational domain, namely

$$
\begin{aligned}
\boldsymbol{\nabla\cdot}\,\boldsymbol{\sigma} - \beta\eta &= f, && \text{in } \mathcal{T}_h, && \text{(3a)}\\
\mathbf{Q}\boldsymbol{\sigma} + \boldsymbol{\nabla}\eta &= \mathbf{0}, && \text{in } \mathcal{T}_h, && \text{(3b)}\\
[\![\boldsymbol{\sigma}\boldsymbol{\cdot}\boldsymbol{n}]\!] &= 0, && \text{on } \mathcal{E}_h^i, && \text{(3c)}\\
[\![\eta\, \boldsymbol{n}]\!] &= \mathbf{0}, && \text{on } \mathcal{E}_h^i, && \text{(3d)}
\end{aligned}
$$

with $f = s_x s_y B(\eta_0)$, $\beta = k^2 s_x s_y c c_g$ and $\mathbf{Q} = (c c_g \mathbf{P})^{-1}$. The jump operator $[\![\cdot]\!]$ is defined in [47] with the normal explicitly written to clarify the nature of the resulting function. The discrete weak form is then stated for each element K: find $\boldsymbol{\sigma}_h \in \boldsymbol{V}_h$, $\eta_h \in P_h$ and $\lambda \in M_h$ such that

$$
\begin{aligned}
-\left(\boldsymbol{\sigma}_h, \boldsymbol{\nabla} q\right)_K - \left(\beta\eta_h, q\right)_K + \left\langle\hat{\boldsymbol{\sigma}} \cdot \boldsymbol{n}, q\right\rangle_{\partial K} &= \left(f, q\right)_K && \forall q \in P_h, && \text{(4a)}\\
\left(\mathbf{Q}\boldsymbol{\sigma}_h, \boldsymbol{v}\right)_K - \left(\eta_h, \boldsymbol{\nabla\cdot}\,\boldsymbol{v}\right)_K + \left\langle\lambda, \boldsymbol{v} \cdot \boldsymbol{n}\right\rangle_{\partial K} &= 0 && \forall \boldsymbol{v} \in \boldsymbol{V}_h, && \text{(4b)}
\end{aligned}
$$

where $\hat{\boldsymbol{\sigma}}$ is a numerical flux and the subscript h is used to note that the unknowns of the problem have been replaced by their discretized counterpart. Equation (3d) has been imposed in weak form replacing the trace of η in (4b) by the new variable $\lambda \in M_h$, which is single valued in each edge. The problem is closed imposing equation (3c) for each interior edge, and the boundary conditions (2b) and (2c),

$$\left\langle \hat{\boldsymbol{\sigma}} \cdot \boldsymbol{n}, \mu \right\rangle_{\partial \mathcal{T}_h} + i \left\langle cc_g k \alpha \lambda, \mu \right\rangle_{\Gamma_{\mathrm{R}}} + i \left\langle cc_g k \lambda, \mu \right\rangle_{\Gamma_{\mathrm{NRB}}} = \left\langle cc_g \left(\boldsymbol{\nabla} \eta_0 \cdot \boldsymbol{n} - ik\alpha\eta_0 \right), \mu \right\rangle_{\Gamma_{\mathrm{R}}}. \tag{4c}$$

As specified in [35], the numerical flux is set in terms of λ as

$$\hat{\boldsymbol{\sigma}} = \boldsymbol{\sigma}_h + \tau(\eta_h - \lambda)\boldsymbol{n}, \tag{5}$$

where τ is a positive stabilization parameter.

Note that, differently from other mixed methods, the same polynomial degree can be used for the space of the primal unknown, P_h, and the space of its gradient, $\boldsymbol{V}_h$. This is due to the particular form of the numerical fluxes (5), that provide stabilization to the formulation without the need of an enriched space for the gradient variable.

The coefficient τ is a positive stabilization parameter, whose influence on the convergence properties of the HDG method has been studied in [35, 48, 39]. It may be prescribed as a positive value on every edge of each triangular element (*all faces* approach) [48, 39], or may be set to zero except on a single arbitrary chosen edge of each element (*single face* approach) [35]. Both options require τ to be large enough for stability, and both provide, for properly chosen values of τ, optimal convergence in the solution η and its gradient $\boldsymbol{\sigma}$, viz. order $p+1$ in $\mathcal{L}_2$ norm. More precisely, extensive numerical evidence [35, 39] shows that values of order one provide optimal behavior for a dimensionless problem. Nevertheless, the single face approach presents an increased robustness for the choice of τ, it allows using larger values without any remarkable impact in the solution, see the numerical study in Appendix A. This is not the case for the all faces approach. When large values of τ are prescribed in every edge superconvergence of the post-processed solution can be lost. Note that this behavior induces an extra difficulty for equations with non-constant coefficients, such as (2), because τ should vary in each element to account for the variability of the coefficients. In conclusion, the single face stabilization parameter is considered here, that is

$$\tau = \begin{cases} 0, & \text{on } \partial K \backslash \partial K^\tau \\ \tau_K, & \text{on } \partial K^\tau \end{cases} \qquad \forall K \in \mathcal{T}_h \tag{6}$$

with a constant $\tau_K > 0$, and ∂K^τ an arbitrary edge of element K. A constant value τ_K is used for all the elements, and a simple dimensional analysis leads to the following expression for the minimum value of τ_K to be used

$$\tau_K \approx \max_{\Omega} \{ kcc_g |s_x / s_y| \}. \tag{7}$$

Note that τ is defined element-by-element, thus an edge shared by two elements may have two different values of τ.

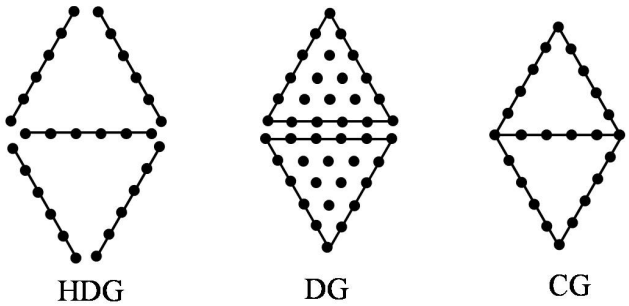

Figure 2. Degrees of freedom in a two element mesh of degree 5 for HDG, DG and CG.

Replacing the numerical flux (5) in the weak form defined by equations (4), and following [35], the HDG method for the MSE becomes: find $(\boldsymbol{\sigma}_h, \eta_h, \lambda) \in \boldsymbol{V}_h \times P_h \times M_h$ such that

$$\left.\begin{aligned} \left(\boldsymbol{\nabla}\cdot\boldsymbol{\sigma}_h, q\right)_K - \left(\beta\eta_h, q\right)_K + \left\langle \tau(\eta_h - \lambda), q\right\rangle_{\partial K} &= \left(f, q\right)_K, \\ \left(\mathbf{Q}\boldsymbol{\sigma}_h, \boldsymbol{v}\right)_K - \left(\eta_h, \boldsymbol{\nabla}\cdot\boldsymbol{v}\right)_K + \left\langle \lambda, \boldsymbol{v}\cdot\boldsymbol{n}\right\rangle_{\partial K} &= 0, \end{aligned}\right\} \qquad \forall K \in \mathcal{T}_h, \tag{8a}$$

$$\begin{aligned} \left\langle \left(\boldsymbol{\sigma}_h\cdot\boldsymbol{n} + \tau(\eta_h - \lambda)\right), \mu\right\rangle_{\partial\mathcal{T}_h} + i\left\langle cc_g k\alpha\lambda, \mu\right\rangle_{\Gamma_{\mathrm{R}}} \\ + i\left\langle cc_g k\lambda, \mu\right\rangle_{\Gamma_{\mathrm{NRB}}} = \left\langle cc_g\left(\boldsymbol{\nabla}\eta_0\cdot\boldsymbol{n} - ik\alpha\eta_0\right), \mu\right\rangle_{\Gamma_{\mathrm{R}}}, \end{aligned} \tag{8b}$$

for all $(\boldsymbol{v}, q, \mu) \in \boldsymbol{V}_h \times P_h \times M_h$.

Note that, on one hand, (8a) is a local system in each element K that does not involve unknowns of neighboring elements. Thus, (8a) can be solved element-by-element to express $\boldsymbol{\sigma}_h$ and η_h as functions of λ. On the other hand, equation (8b) is a global equation coupling variables of different elements. Replacing $\boldsymbol{\sigma}_h$ and η_h, solution of (8a) in terms of λ, in (8b) yields a global system on the whole mesh skeleton for only one variable: the trace $\lambda \in M_h$. Recall that λ is single valued in each edge F of the mesh. Once the global system is solved, $\boldsymbol{\sigma}_h$ and η_h, can be recovered for each element K using (8a).

Figure 2 compares schematically the location and number of DOF on two triangles interpolated with polynomials of degree five for the HDG method, a standard DG method, such as CDG [31], and CG with, obviously, static condensation of the interior nodes. Compared to other DG methods, the hybridization technique in HDG reduces drastically the number of DOF for high-order approximations. With respect to CG, HDG has more unknowns due to the replication of vertex nodes. However, the counterpart of this little increase in DOF is the flexibility of the discontinuous approximation, which is advantageous for p-adaptivity, and the interesting super-convergence properties of HDG.

For a uniform p distribution, HDG with the particular choice of the numerical flux proposed in (5) obtains optimal convergence rates of order $p+1$ in the L_2 norm, for the unknown η_h and also for its derivative $\boldsymbol{\sigma}_h$, see [35]. This property is the key ingredient for a local element-by-element post-process of the HDG solution. Knowing $\boldsymbol{\sigma}_h$ in the interior of each element and the equilibrated fluxes on the edges with a $p+1$ accuracy allows solving the differential equation (3b) for the reflected surface elevation function. A new problem is defined from the divergence of (3b)

with the corresponding boundary condition, namely

$$-\boldsymbol{\nabla}\cdot(\nabla\eta_h^*) = \boldsymbol{\nabla}\cdot(\mathbf{Q}\boldsymbol{\sigma}_h) \quad \text{in } K, \tag{9a}$$

$$-\nabla\eta_h^*\cdot\boldsymbol{n} = \mathbf{Q}\boldsymbol{\sigma}_h\cdot\boldsymbol{n} \quad \text{on } \partial K. \tag{9b}$$

where $\eta_h^* \in \mathcal{P}^{p+1}(K)$, $\forall K \in \mathcal{T}_h$. This Neumann problem requires for solvability the additional constraint:

$$\int_K \eta_h^*\, d\Omega = \int_K \eta_h\, d\Omega. \tag{10}$$

This provides a super-convergent solution η_h^* with errors of order $p+2$ in L_2 norm. The weak form associated to equations (9) with constrain (10) is

$$\begin{aligned}\left(\nabla\eta_h^*, \nabla q\right)_K &= -\left(\mathbf{Q}\boldsymbol{\sigma}_h, \nabla q\right)_K \quad \forall q \in \mathcal{P}^{p+1}(K),\\ \left(\eta_h^*, 1\right)_K &= \left(\eta_h, 1\right)_K,\end{aligned}$$

to be solved in a element-by-element fashion.

In case of non-uniform distributions of p_K, for each element K the post-process solution η_h^* belongs to the corresponding increased space, i.e. $\eta^* \in \mathcal{P}^{p_K+1}(K)$. The super-convergence property for the HDG post-processed solution is only proved for a uniform p distribution. Nevertheless, numerical experiments confirm that the element-by-element post-process solution for non-uniform p distributions improves the accuracy of the computation. Thus, here the post-process solution is used to obtain an error estimate in each element through a low cost element-by-element computation.

4. ERROR ESTIMATION AND *P*-ADAPTIVE ALGORITHM

To ensure the quality of the FE solution, the accuracy of the computation must be evaluated and controlled [49]. A posteriori computable error estimates are used to drive the adaptive process. Two different approaches can be used for assessing the error: error indicators or error estimators, see [50] for a general discussion. Error indicators are cheap to evaluate but, in general, are designed for a specific problem and do not provide error bounds. Error estimators are more accurate and general, can be used in linear and nonlinear problems, for instance [51], and can even produce bounds of the exact solution [52, 53, 54, 55]. But a posteriori error estimators have a non trivial computational overhead when recovery techniques are used [56], or when equilibrated fluxes must be computed [57] and also in flux-free implementations [58]. Therefore, the super-convergent post-process inherent in HDG is a important asset, which can be readily employed to estimate the error. In the case of uniform p_K the HDG post-process provides an asymptotically exact estimator [38], in case of a non-uniform p_K distribution, numerical examples confirm the reliability of this estimator.

The usual output for the engineering application considered here is the *wave amplification factor*. That is, the ratio between the total wave-height, $H = |\eta + \eta_0|$, and incident one, $H_0 = |\eta_0|$. The latter is usually normalized given the linearity of the problem. Consequently, a measure of the wave-height error in the domain of interest, $\Omega_{\texttt{int}}$ (typically the area of interest in the interior of

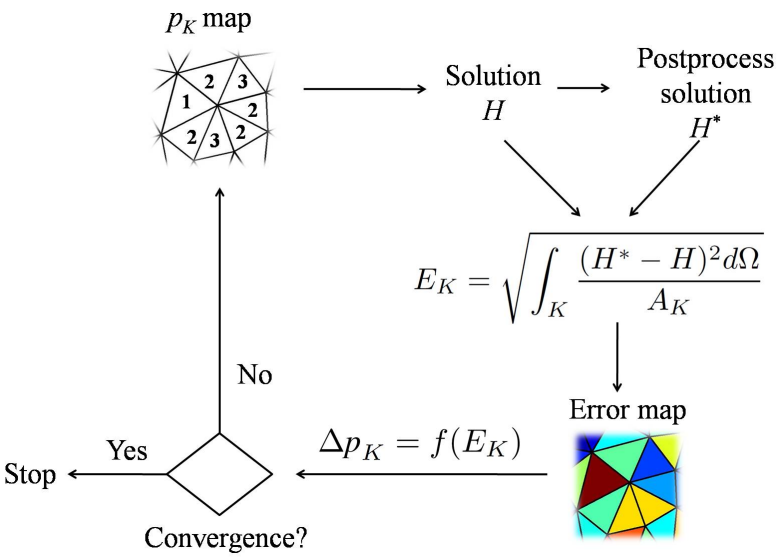

Figure 3. Schematic representation of the adaptive strategy

the harbor) is prescribed below a user-given tolerance, ε, namely

$$\max\{E_K | K \in \Omega_{\text{int}}\} = E_{\text{int}} \leq \varepsilon \tag{11a}$$

with E_K being the error in element K, that is

$$E_K^2 = \frac{1}{A_K} \int_K \left(\frac{H^* - H}{H_0} \right)^2 d\Omega, \tag{11b}$$

where H^* is the super-convergent wave-height (i.e. the post-processed solution) and A_K the area of element K. Instead of a point-wise error, here, the $\mathcal{L}_2$ norm is used in each element. Moreover, in contrast with [59], the local elemental contribution is normalized by the element area [60]. This error measure is bounded by the user-defined tolerance, and the post-process solution in HDG only requires local computations. It is important to note that in wave problems, local adaptivity in Ω_{int} cannot lead to this goal because of pollution errors [61].

The adaptive strategy proposed here and schematically presented in Figure 3 is inspired from [62]. An iterative process is defined aiming at complying with (11). This process is based on estimating the variation in the approximation order for each element in the computational domain to reach the desired accuracy in the area of interest. Given an approximation obtained with a p_K-map of interpolation degrees, a p increment, Δp_K, is evaluated for every element, i.e. $\forall K \in \mathcal{T}_h$. The desired p_K variation in each element is computed as

$$\Delta p_K = \left\lceil \log_b(E_K/\epsilon_K) \right\rceil, \tag{12}$$

where $\lceil \cdot \rceil$ denotes the *ceiling* function, that is, a function that maps a real number to the smallest following integer. Note that ϵ_K, which can be different for each element, is a user-given tolerance prescribing a desired element-error. Here, $\epsilon_K = \varepsilon/\gamma$ for all elements in the area of interest Ω_{int} and $\epsilon_K = \gamma\varepsilon$ for all elements in $\Omega \setminus \Omega_{\text{int}}$, with a parameter $\gamma > 1$. Thus, the refinement is intensified

to reach the desired accuracy in the area of interest Ω_{int}, and relaxed outside to reduce the computational effort. A parameter $\gamma = 2$ has been used in the selected numerical tests, but good results have been observed for $\gamma \in]1, 2]$.

As noted in [62] the logarithm base b also controls the behavior of the adaptive scheme. For a fixed elemental error ratio E_K/ϵ_K, increasing b has the obvious effect of decreasing Δp_K. Thus, small values of b yield drastic variations in the polynomial orders of the elements. This may reduce the number of iterations until convergence but it can also produce a oscillatory p_K-map around the optimal one. On the contrary, large values of b yield slow p variations, the number of iterations to determine the optimal p_K-map is increased but it converges to the optimal map without undesired oscillations. The optimal value of b depends on the prescribed tolerance ε. In the examples studied here, good behavior was btained for $10 \leq b \leq 100$, which corresponds to increase p by 1, i.e. $\Delta p = 1$, for $E_K/\epsilon_K = 10$ and 100 respectively.

In addition, an upper and lower bound for the order of approximation is usually defined, namely $p^- \leq p_K \leq p^+$. Defining a suitable number of elements per wavelength is not a trivial task. A "rule of thumb" usually suggests 10 linear elements per wavelength [63, 64] and, obviously, less than 4 linear elements is impossible. To roughly estimate p^- and p^+, assume that high-order elements require the same number of nodes per wavelength than linear ones, which is on the safe side because as noted in [63] high-order elements require less nodes per wavelength. Since the number of nodes per one wavelength is $1 + p(2\pi)/kh$ where h is the characteristic element size. A reasonable upper bound for the degree of approximation can be estimated with $p^+ \approx 10kh/2\pi$ and an absolute lower bound by $p^- \approx 4kh/2\pi$. Note however that results are very insensitive to the prescribed lower bound because the adaption process puts enough nodes even if a lower value for p^- is prescribed. On the contrary, the upper bound, which limits the maximum polynomial degree in the mesh, may have an influence in the results if the elements are excessively large (for the desired tolerance and the solution wavelengths). This can be avoided with an hp adaptive strategy. For the problem at hand, h refinement was unnecessary even for very large elements (a characteristic element size equal to incoming wavelength, i.e. $kh \approx 2\pi$) provided engineering accuracy was imposed (i.e. approximately two significant digits) and $p^+ = 10$, as suggested from the previous safe estimate.

Finally, it is important to note that in order to avoid drastic variations in the order of the approximation, the difference in polynomial order between two neighboring elements is not greater than a given value δ. This value is set to one as in [59] to avoid spurious wave reflections. Nevertheless, the smoothing algorithm that imposes a maximum jump of δ is such that it ensures for every element K that the retained value for the approximation is $\max\{p_K + \Delta p_K, p^{\text{neighbor}} - \delta, p^-\}$ where p^{neighbor} is the maximum order in any element sharing an edge with K.

The computation is typically carried out in the first stage on a uniform mesh with $p_K = p^-$ and the iterative adaptation scheme stops when the prescribed precision ε is attained in the area of interest. Failure to converge to the desired accuracy is considered when in two successive iterations the percentage of elements changing their order is lower than a given tolerance and, obviously, the target ε is not accomplished.

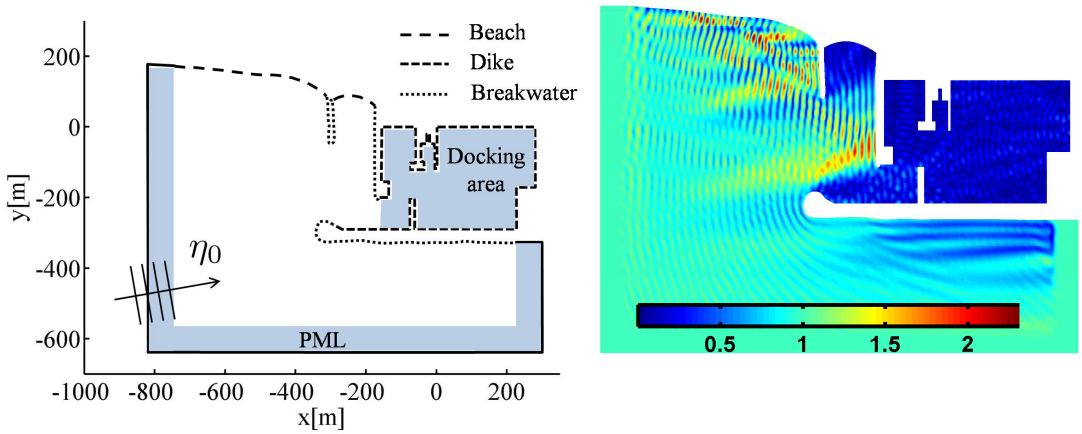

Figure 4. Problem statement for Mataro's harbor (left) and wave amplification factor solution (right)

5. NUMERICAL RESULTS

The performance of the proposed adaptive HDG method is studied in real applications. One is a medium size harbor (Mataro's harbor) the other is a large one (Barcelona's harbor). HDG adaptive solutions are compared with high-order CG solutions, assessing the efficiency of the method in terms of number of DOF of the linear system for the same accuracy in the area of interest. Obviously, no analytical solution are available for these examples. The errors are computed using the proposed error estimator for HDG. For CG and CDG the reference solution is computed on a $p+1$ mesh. Note that the computational overhead for CG and CDG is non-negligible and it is not introduced in the comparisons. The efficiency of the HDG error estimator is also evaluated in the two test cases. To do so, a reference solution is evaluated in each case with a high-order CG approximation on an h-refined mesh. Since discretization errors are of concern here, the PML region is kept unchanged in every computation, also for the reference computation.

5.1. Mataro harbor

Figure 4 (left) depicts the first problem statement, note that the PML region is highlighted. The docking area is considered as the area of interest and it is shown in Figure 4. The physical boundaries are also indicated, they are modeled as absorbing boundaries with $\alpha = 0.02$ for dikes, $\alpha = 0.4$ for breakwaters, and $\alpha = 0.7$ for beaches. The incident wave direction is 10° from the x-axis, which should induce strong agitation in the interior. The wave period is 5s, corresponding to short waves with a maximum value of the wavelength of about 40m in the PML region, and a minimum value of 25m in the interior of the harbor and close to the beach. Real bottom depth has been used everywhere except in the PML region where constant depth is imposed. A high-order meshing software [65] is used to generate an unstructured triangular mesh with a uniform characteristic size $h \approx 40$m everywhere in domain, except for the interior of the harbor where the mesh size is adapted locally to capture all the relevant geometrical features of the docking area.

The wave amplification factor in the domain is also displayed in Figure 4 (right). Note the increase of the wave-height (amplification factors larger than two) due to the bathymetry in the harbor

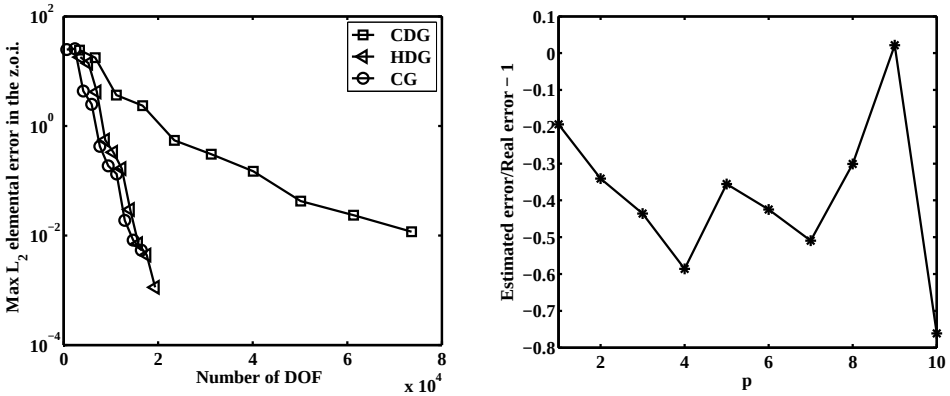

Figure 5. Error vs. DOF for non-adaptive, i.e. uniform p (left), for HDG, CG and CDG. Efficiency of the error estimator in HDG (right).

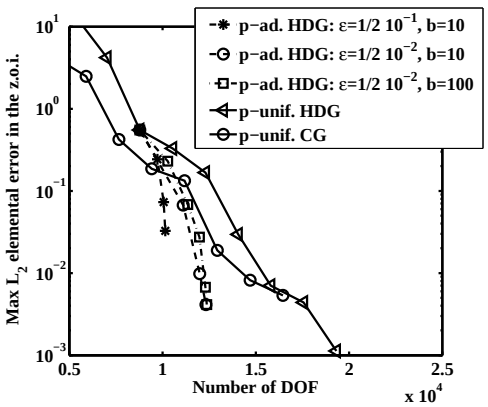

Figure 6. Zoomed convergence curves for p-uniform CG and HDG and p-adaptive HDG computations.

entry and on the beach outside the harbor. Figure 5 (left) shows the convergence of the maximum elemental wave-height $\mathcal{L}_2$ error in the area of interest, i.e. $E_{\texttt{int}}$ see (11a), versus the number of DOF. Each mark of the convergence curves corresponds to a simulation with uniform p; along each curve p increases from 1 to 10 on the same mesh for CDG, HDG and CG. Observe that CG is always more efficient (in terms of DOF) than non-adaptive DG methods for a similar accuracy. CDG is drastically penalized by the interior element nodes. However, as expected, the number of DOF for HDG is close to CG as p increases. In HDG only the vertices of the triangulation are repeated and this penalizes low-order approximations. Note however, that run-time comparisons may be advantageous for HDG at mid to high-orders because the structure of the information (constant bandwidth of block dense matrices) allows important gains in today's hardware, see for instance [39].

In Figure 5 (right), the efficiency of the error estimator used in HDG is evaluated for each computation. The estimator efficiency is defined as $\left(E_{\texttt{int}}/\max\{\tilde{E}_K|K\in\Omega_{\texttt{int}}\}\right)-1$, where $\tilde{E}_K$ is the "real" elemental error; that is, the error computed with the reference solution (an overkilled h-refined CG solution). The graphic shows that, in this case, the estimator is almost always underestimating $E_{\texttt{int}}$. Moreover, the efficiency is, for most of the range of p larger than $1/2$. Comparisons with three different strategies of p-adaptive HDG solutions are depicted in Figure 6. To better appreciate the improvements, a zoom, with respect to the left figure, is shown and only

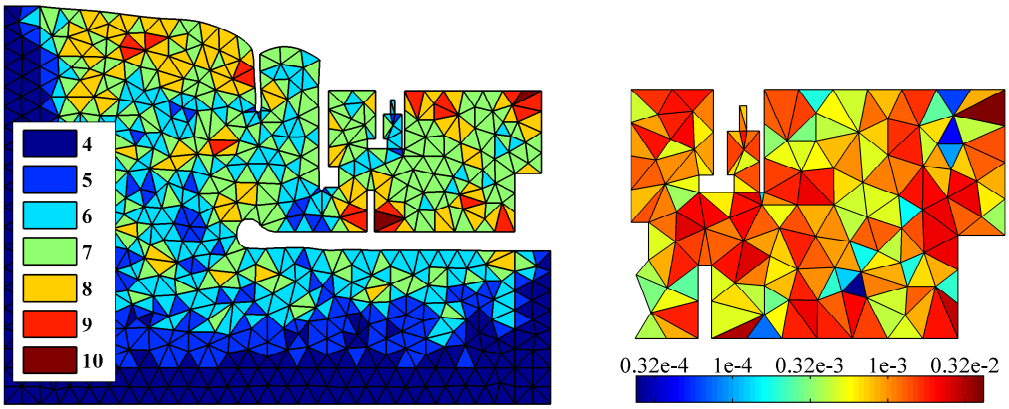

Figure 7. Adaptive results for $\varepsilon = 0.5\,10^{-2}$, p-map (left) and error map in area of interest (right)

the HDG and CG methods are plotted. Without recourse to computational efficiency of the different schemes, p-adaptive HDG requires less DOF for a given accuracy compared with uniform CG. No CG p adaptivity is compared because it is clearly more cumbersome to implement than in DG. This figure illustrates the convenience of the p-adaptive technique, which allows to reduce considerably the DOF of the computation, providing better performance than uniform CG approximations. This test also shows the reliability of the error estimator in the task of driving an adaptive process.

This results are obtained with the methodology proposed in Section 4 and imposing two different tolerances $\varepsilon = 0.5\,10^{-1}$ and $\varepsilon = 0.5\,10^{-2}$ (i.e. one and two significant digits [66], which cover the usual engineering accuracy needs). The targeted elemental tolerance ϵ_K was prescribed imposing $\gamma = 2$. Since an almost uniform element size was is imposed equal to the incident wave length, i.e. $h \approx 2\pi/k_0 = 40$m, the lower bound for the approximation order is $p^- = 4$ and the upper bound $p^+ = 10$ is never a restriction. Two values of the parameter b, see (12), are also tested for the case $\varepsilon = 0.5\,10^{-2}$, $b = 10$ and $b = 100$, leading to almost the same converging point, the first one with three iterations and the second one with five iterations. As expected lower values of b converge faster. However, as noted earlier, if b is further reduced convergence can be lost, this is the case for $b = 2$. Figure 7 (left) depicts the p_K-map for $\varepsilon = 0.5\,10^{-2}$. Note that high values of p are required in the area of interest but also outside $\Omega_{\texttt{int}}$ where interactions and water depth have an influence in the accuracy in the area of interest. The elemental errors in the area of interest is shown in Figure 7 (right). Obviously, the maximum error is below the prescribed value ε, and the majority of the element stay in a range of error comprised in one order of magnitude. Thus, a reasonably uniform error distribution is achieved.

5.2. Barcelona harbor

In this example, the computational domain covers approximately 34.4km^2, see Figure 8. The ratio between relevant small features, a few meters, and the horizontal dimension of the harbor, 10km, suggest one of the challenges in this case. The computational domain is discretized [65] with 32 802 elements, 5% of which are in the PML area. The unstructured triangular mesh has a prescribed uniform characteristic size $h \approx 50$m in the outer region, which approximately coincides with the incoming wavelength at high depth, while in the interior of the harbor the mesh size is adapted

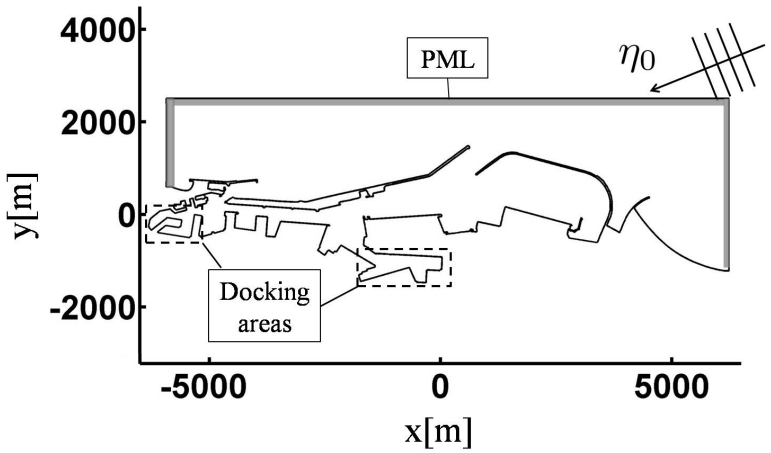

Figure 8. Barcelona harbor: statement of the problem.

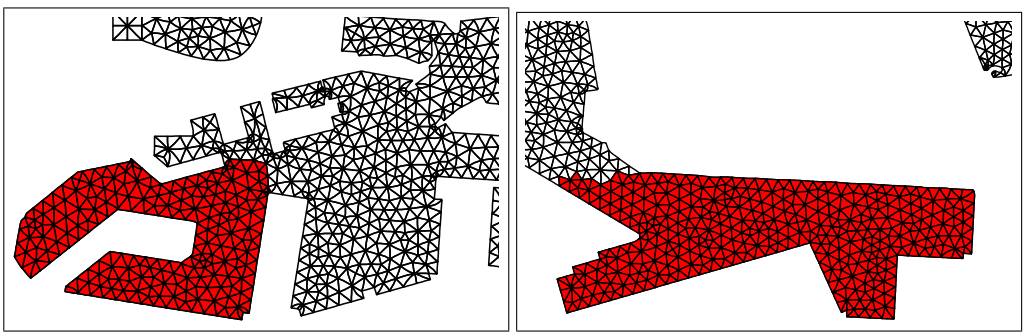

Figure 9. Barcelona harbor: zoom in the areas of interest.

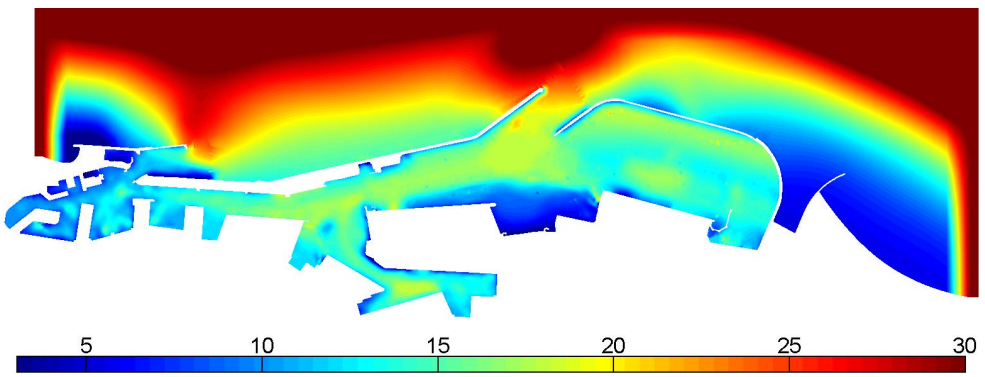

Figure 10. Barcelona harbor: bottom depth

locally to capture all the relevant geometrical features. Figure 8 highlights two non-connected areas of interest and Figure 9 zooms to shown the mesh. To avoid tangled elements and improve the quality of the mesh the technique proposed in [67] is used.

Figure 10 shows a map of the bottom depth. It coincides with actual data except for the vertical left and right boundaries where it is smoothed to simplify the imposition of the PML conditions. The PML region is located away from the area of interest, in a zone where the value of the bottom depth does not affect the wavelength of the incoming wave. The incoming wave has a direction of

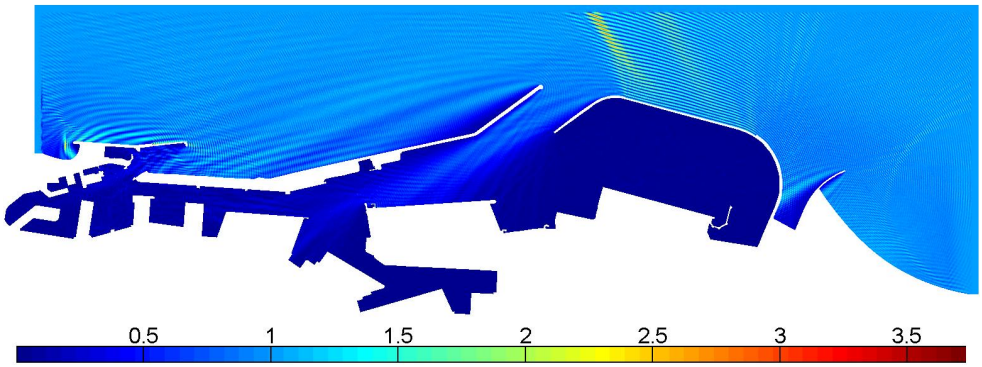

Figure 11. Wave amplification factor in the Barcelona harbor.

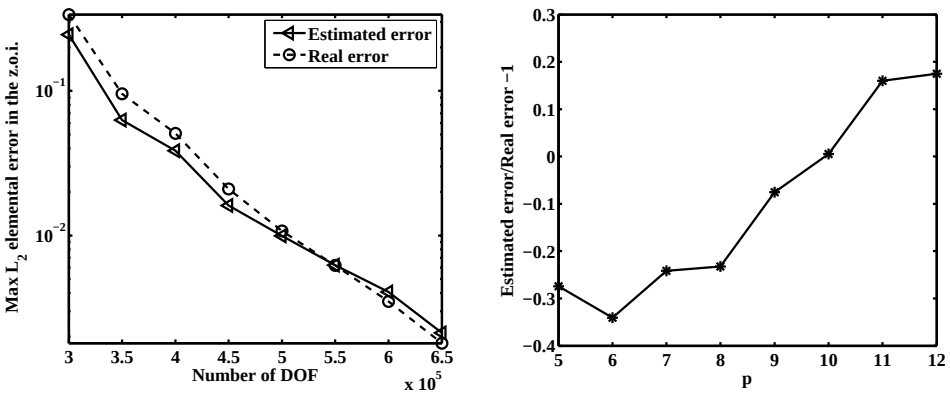

Figure 12. Analysis of the error estimate for the Barcelona harbor and uniform p HDG computations. Comparison between $E_{\texttt{int}}$ and the error computed with a reference solution for $p = 5, \ldots, 12$ (left) and efficiency of the error estimator (right).

202.4° from the x-axis and a period of 6s and, consequently, the incoming wavelength in the outer boundary is 56m. The wave amplification factor is shown in Figure 11. Note that, with the selected period of the incident wave, more than 200 waves are present in the computational domain.

Figure 12 (left) plots $E_{\texttt{int}}$ (the maximum elemental L_2 error in the wave amplification factor for the area of interest) versus the number of DOF of the computation (solid line). Markers are plotted for $p = 5, \ldots, 12$ since p uniform HDG computations are performed. This curve (solid line), based on the estimate of the post-processed solution, can be compared with the "exact" error (dashed line) where the reference solution is obtained with CG, the same mesh, and $p = 20$. Note the good agreement between the estimate and the "exact" error. To further study the estimate Figure 12 (right) shows the efficiency of the error estimator as a function of p for these computations. Again, very good efficiencies are obtained.

For the HDG p-adaptive simulations, the target accuracy is set to $\varepsilon = 10^{-2}$ and $\varepsilon = 0.5\,10^{-2}$, the lower bound for the order of the approximation is $p^- = 5$ and again, there is no need to limit the desired accuracy with an upper cap. To drive the adaptive process the parameter defining the element target error is $\gamma = 2$. Figure 13 shows convergence for p-adaptive HDG and p-uniform HDG and CG computations. For $\varepsilon = 10^{-2}$, only $b = 10$ is considered and convergence is obtained with four iterations of the adaptive process. For $\varepsilon = 0.5\,10^{-2}$, two values for b are compared: $b = 10$

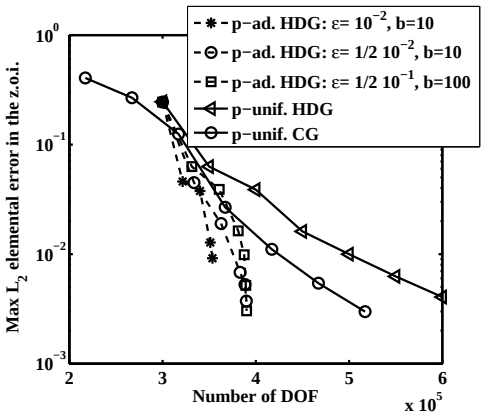

Figure 13. Convergence comparison between p-uniform HDG and CG for $p = 5, \dots, 11$ and three HDG p-adaptive computations.

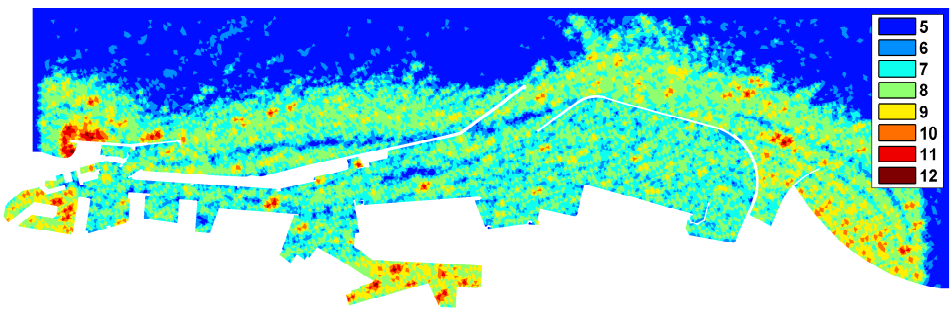

Figure 14. Map of the approximation order p at convergence, for the case $\varepsilon = 0.5\,10^{-2}$ and $b = 10$.

and $b = 100$. As expected less iterations (five) are necessary for the lower b while six iterations are required for $b = 100$. Nevertheless, they both reach similar converged solutions. Note that every adaptive computation induces a significative reduction in number of DOF compared to p-uniform CG and HDG computations. As noted earlier if b is too small, viz. $b = 2$, oscillatory no convergent p-maps can be obtained.

Figure 14 shows the distribution of order p for $\varepsilon = 0.5\,10^{-2}$ and $b = 10$. Note that the maximum p is only imposed in small areas. Moreover, there is a certain correspondence between high p and shallow waters where the wavelength is reduced, see Figure 10. As expected the p-adaptive technique is automatically putting the necessary nodes per wavelength in each part of the domain.

Finally, the elemental errors in the docking area for the case $\varepsilon = 0.5\,10^{-2}$ and $b = 10$ are plotted in Figure 15 with an almost uniform error distribution in the zone of interest.

Table I compares runtime, error and DOF in a p-refinement process for p-uniform CG and p-variable HDG to demonstrate the advantages of the p-adaptive HDG strategy. The desired accuracy is $\varepsilon = 0.5\,10^{-2}$. CG computations use uniform degree p. The error can be estimated with any a posteriori error estimator. Here, for simplicity a new computation with uniform $p + 1$ is done and, obviously, the runtime indicated in Table I for CG only accounts for the first solve with the approximation of order p. For each iteration, the uniform CG degree is updated as the maximum degree in the p-map obtained using (12). The table presents the degree p for each CG computation,

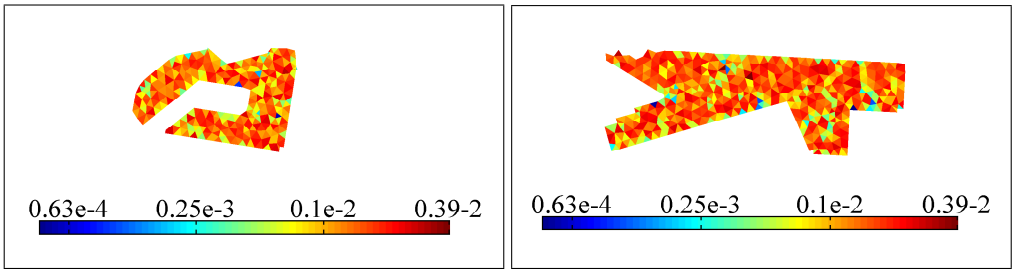

Figure 15. Barcelona harbor: error map in the docking areas.

Table I. Barcelona harbor: runtime, error and DOF comparison for increasing p-uniform CG and p-adaptive HDG the latter with a desired tolerance of $\varepsilon = 0.5\,10^{-2}$ and $b = 10$.

	iteration	0	1	2	3	4
CG	p	5	7	9	10	11
	error	0.40	0.12	$0.11\,10^{-1}$	$0.54\,10^{-2}$	$0.30\,10^{-2}$
	DOF	217 198	317 198	417 198	467 198	517 198
	runtime solve [s]	24	42	113	146	187
HDG	p or its range	5	$5,\ldots,8$	$5,\ldots,10$	$5,\ldots,11$	$5,\ldots,12$
	error	0.24	$0.45\,10^{-1}$	$0.19\,10^{-1}$	$0.64\,10^{-2}$	$0.36\,10^{-2}$
	DOF	300 000	333 832	362 028	380 842	384 951
	runtime solve [s]	64	82	100	115	122
	runtime err. est.[s]	17	27	33	40	42

its corresponding maximum estimated error in the area of interest, the number of DOF and the runtime. Four iterations of this process are needed to attain the desired precision.

HDG uses the proposed methodology described earlier, in this case, with a refinement parameter $b = 10$. The results are also shown in Table I. The first iteration uses the same mesh and $p = 5$ as the first CG iteration. As expected HDG is more computationally expensive than CG but provides better accuracy for the same discretization. Now, however, the post-processed approximation provides a reasonable error estimate with a reduced overhead (one third of the coarse computation), it is also indicated in the table. The following iterations have and adapted p distribution. The table shows the range of p, the maximum $\mathcal{L}_2$ error in the area of interest, the number of DOF, the run-time for the solution and the run-time for the HDG error estimate. Four iterations are also required to attain the desired accuracy and the successive iterations show how the proposed p-adaptive algorithm improves the efficiency of the HDG computations. Note that the sum over the iterations of runtimes is 483 s for HDG and 512 s for CG and that any error estimator for CG will be more computationally expensive than the post-process of HDG.

6. CONCLUDING REMARKS

The Hybridizable Discontinuous Galerkin method is applied to harbor agitation problem, which requires solving the Helmholtz equations with non-constant coefficients in an unbounded domain. The hybridization technique allows to reduce drastically the number of degrees of freedom of the computation because the system of equations only involves unknowns on the element edges.

Moreover, it opens the path to an inexpensive super-convergent post-processed solution that characterizes an error estimate. This error estimate is centered in an engineering quantity of interest: the wave height. The error estimator is used to, on one hand, prescribe a desired accuracy in the zone of interest of the domain and, on the other hand, to drive an iterative procedure of mesh adaptation. The proposed strategy both for the stabilization of HDG as well as for the adaption strategy shows good results in two engineering wave propagation studies in real harbors. Fast convergence to the desired level of precision is shown. The number of degrees of freedom for the proposed p-adaptive HDG method is below the high-order continuous finite element method (with, obviously, static condensation for the interior nodes) at a given accuracy. Moreover, the proposed approach incorporates an inexpensive error estimate. which is not the case for continuous Galerkin. This, is to the authors knowledge, one of the first real engineering applications where discontinuous Galerkin is shown to outperform continuous Galerkin.

ACKNOWLEDGEMENT

Bathymetry data for the Barcelona harbor comes from a real campaign of measure courtesy of the *Autoritat Portuaria de Barcelona*.

A. INFLUENCE OF THE STABILIZATION PARAMETER IN HDG CONVERGENCE

The convergence properties of HDG with *single face* stabilization parameter are studied here, for different values of τ_K in equation (6). A scattering problem with analytical solution [68] is used for this analysis: a plane wave is propagated over an constant horizontal bottom and scattered by a cylindrical object of unitary radius. Figure 16 plots the convergence of the exact L_2 error over the whole domain as the element size decreases for the standard HDG solution (solid line) and its post-processed result (dashed line). Moreover, this is done for different values f the degree of approximation $p = 1, \dots, 4$. The mean convergence rate isdisplayed at the end of each convergence curve. Four graphics are shown, one for each tested value of τ_K, namely $\tau_K = 10^n$ for $n = 0, \dots, 3$. As expected, the convergence characteristics improve as the parameter τ_K increases. But recall that very large stabilization parameters affect the conditioning of the system of equations. It is very important to note that the value provided by equation (7) in this case is approximately 50, which falls perfectly in the well-behaved range for τ_K.

Since p-variable discretizations are of concern in this work, the influence of τ_F varying with p is studied next. To this end, Figure 17 shows p-convergence curves for $\tau_K = 10^n p^\gamma$ with $n = 0, \dots, 3$ and $\gamma = \{1, 0, -1\}$. The major conclusion from these curves is that there is no improvement in imposing a τ_K varying with p. The three cases behave similarly and this is important for a p-adaptive computation because τ_K can be independent on the actual p_F used on each mesh edge.

REFERENCES

1. Chang C. A least-squares finite element method for the Helmholtz equation. *Comput. Methods Appl. Mech. Eng.* 1990; **83**(1):1–7.
2. Harari I, Hughes TJR. Galerkin/least-squares finite element methods for the reduced wave equation with nonreflecting boundary conditions in unbounded domains. *Comput. Methods Appl. Mech. Eng.* 1992; **98**(3):411–454.
3. Babuška I, Sauter SA. Is the pollution effect of the FEM avoidable for the Helmholtz equation considering high wave numbers? *SIAM Rev.* 2000; **42**(3):451–484.

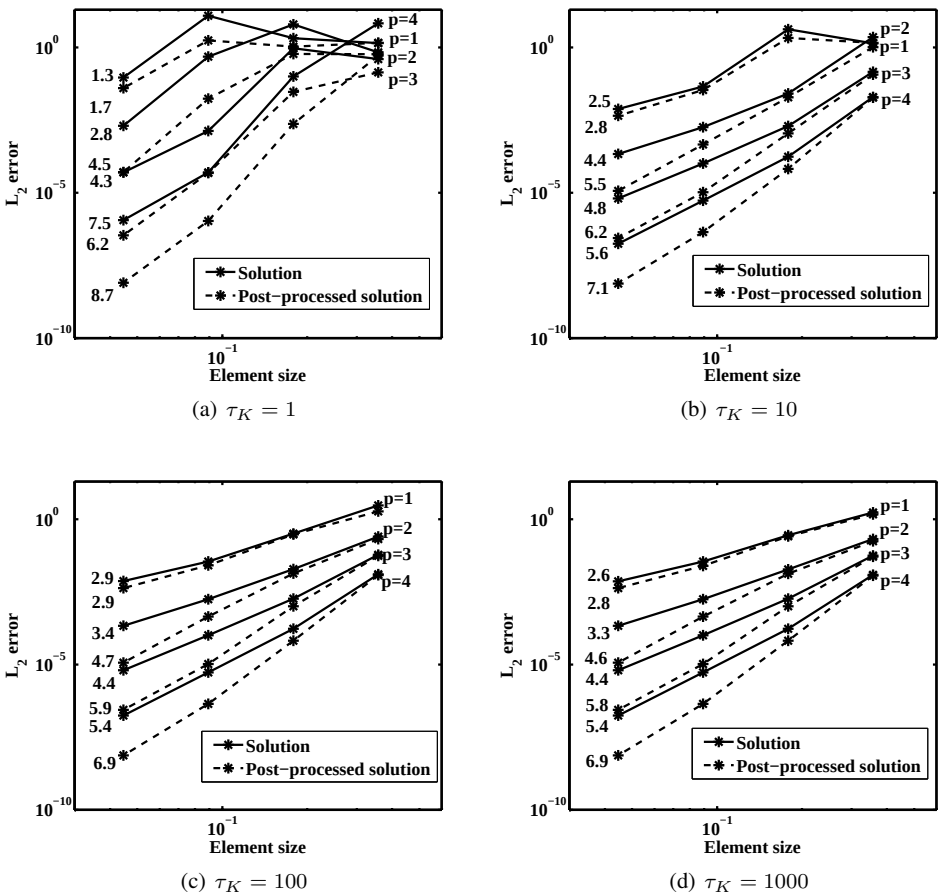

(a) $\tau_K = 1$ (b) $\tau_K = 10$

(c) $\tau_K = 100$ (d) $\tau_K = 1000$

Figure 16. Influence of the parameter τ_K on the h-convergence for a cylindrical scattering problem with constant bottom. The L_2 error for the approximate solution and the post-processed solution are plotted as a function of the element size, for $p = 1, \ldots, 4$.

4. Harari I, Magoulès F. Numerical investigations of stabilized finite element computations for acoustics. *Wave Motion* 2004; **39**(4):339–349.
5. Harari I, Gosteev K. Bubble-based stabilization for the Helmholtz equation. *Int. J. Numer. Methods Eng.* 2007; **70**(10):1241–1260.
6. Melenk J, Babuška I. The partition of unity finite element method: Basic theory and applications. *Comput. Meth. Appl. Mech. Eng.* 1996; **139**(1–4):289–314.
7. Cessenat O, Despres B. Application of an ultra weak variational formulation of elliptic PDEs to the two-dimensional Helmholtz problem. *SIAM J. Numer. Anal.* 1998; **35**(1):255–299.
8. Lacroix V, Bouillard P, Villon P. An iterative defect-correction type meshless method for acoustics. *Int. J. Numer. Methods Eng.* 2003; **57**(15):2131–2146.
9. Farhat C, Harari I, Hetmaniuk U. A discontinuous Galerkin method with Lagrange multipliers for the solution of Helmholtz problems in the mid-frequency regime. *Comput. Methods Appl. Mech. Eng.* 2003; **192**(11-12):1389–1419.
10. Strouboulis T, Hidajat R. Partition of unity method for Helmholtz equation: q-convergence for plane-wave and wave-band local bases. *Appl. Math.* 2006; **51**(2):181–204.
11. Gabard G. Discontinuous Galerkin methods with plane waves for time-harmonic problems. *J. Comput. Phys.* 2007; **225**(2):1961–1984.
12. Gabard G, Gamallo P, Huttunen T. A comparison of wave-based discontinuous Galerkin, ultra-weak and least-square methods for wave problems. *Int. J. Numer. Methods Eng.* 2011; **85**(3):380–402.

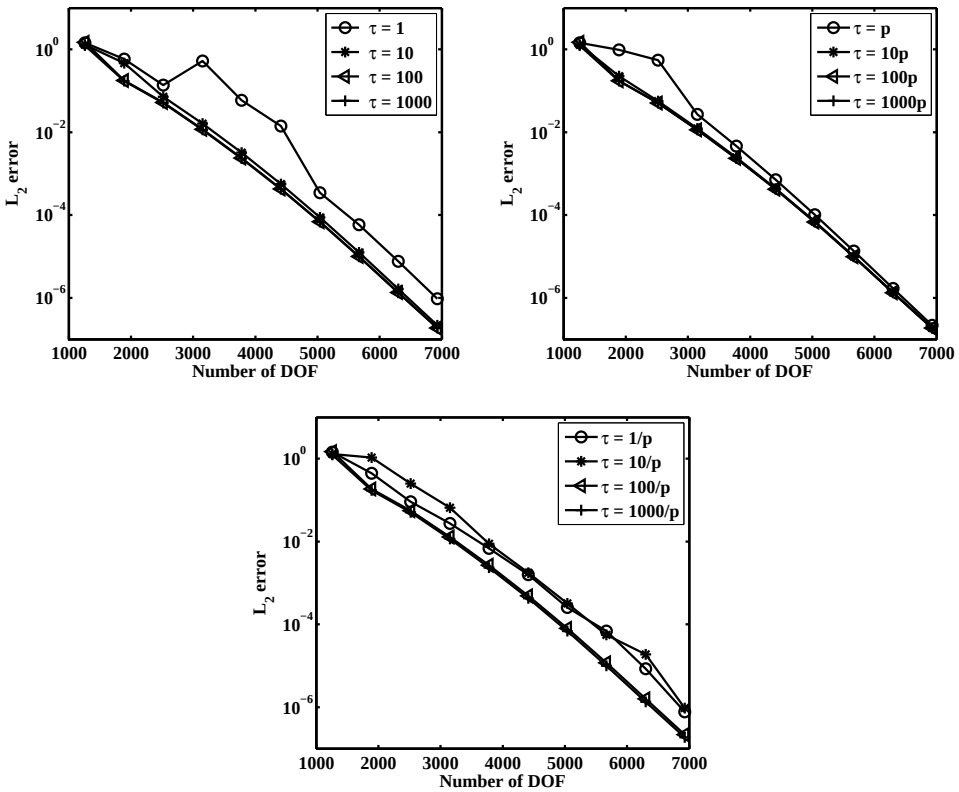

Figure 17. Influence of a p varying τ_K on the p-convergence for a cylindrical scattering problem with constant bottom. The L_2 error for the approximate solution and the post-processed solution are plotted for $p = 1, \ldots, 10$ and constant element size.

13. Panchang VG, Pearce BR, Wei G, Cushman-Roisin B. Solution of the mild-slope wave problem by iteration. *Appl. Ocean Res.* 1991; **13**(4):187–199.
14. Li B, Anastasiou K. Efficient elliptic solvers for the mild-slope equation using the multigrid technique. *Coast. Eng.* 1992; **16**(3):245–266.
15. Bettess P, Zienkiewicz OC. Diffraction and refraction of surface waves using finite and infinite elements. *Int. J. Numer. Methods Eng.* 1977; **11**(8):1271–1290.
16. Liu SX, Sun B, Sun ZB, Li JX. Self-adaptive FEM numerical modeling of the mild-slope equation. *Appl. Math. Model.* 2008; **32**(12):2775–2791.
17. Naserizadeh R, Bingham HB, Noorzad A. A coupled boundary element-finite difference solution of the elliptic modified mild slope equation. *Eng. Anal. Bound. Elem.* 2011; **35**(1):25–33.
18. Houston JR. Combined refraction and diffraction of short waves using the finite element method. *Appl. Ocean Res.* 1981; **3**(4):163–170.
19. Hurdle DP, Kostense J, van den Bosch P. Mild-slope model for the wave behaviour in and around harbours and coastal structures in areas of variable depth and flow conditions. *Advances in water modelling and measurement*. M.H. Palmer, Editor: The Fluid Engineering Centre,Cranfield, Bedford, England, 1989; 307–324.
20. Vos PEJ, Sherwin SJ, Kirby RM. From h to p efficiently: implementing finite and spectral/hp element methods to achieve optimal performance for low- and high-order discretisations. *J. Comput. Phys.* 2010; **229**(13):5161–5181.
21. Cantwell CD, Sherwin SJ, Kirby RM, Kelly PHJ. From h to p efficiently: selecting the optimal spectral/hp discretisation in three dimensions. *Math. Model. Nat. Phenom.* 2011; **6**(3):84–96.
22. Huerta A, Roca X, Aleksandar A, Peraire J. Are High-order and Hybridizable Discontinuous Galerkin methods competitive? *Oberwolfach Rep.* 2012; **9**(1):485–487, doi:10.4171/OWR/2012/09. Abstracts from the workshop held February 12–18, 2012, Organized by Olivier Allix, Carsten Carstensen, Jörg Schröder and Peter Wriggers, Oberwolfach Reports. Vol. 9, no. 1.

23. Modesto D, Giorgiani G, Zlotnik S, Huerta A. Efficiency and accuracy of high-order computations and reduced order modelling in coastal engineering wave propagation problems. *Proceedings of the ECCOMAS Young Investigators Conferences 2012*, Aveiro, Portugal, 2012.
24. Giorgiani G, Fernández-Méndez S, Huerta A. Hybridizable discontinuous Galerkin p-adaptivity for wave problems. *Proceedings of the ECCOMAS Young Investigators Conferences 2012*, Aveiro, Portugal, 2012.
25. Sevilla R, Hassan O, Morgan K. An analysis of the performance of a high-order stabilised finite element method for simulating compressible flows. *Comput. Methods Appl. Mech. Eng.* 2013; **253**(0):15–27, doi:10.1016/j.cma.2012.09.001.
26. Shephard M, Dey S, Flaherty J. A straightforward structure to construct shape functions for variable p-order meshes. *Comput. Methods Appl. Mech. Eng.* 1997; **147**(3-4):209–233.
27. Devloo PRB, Bravo CMAA, Rylo EC. Systematic and generic construction of shape functions for p-adaptive meshes of multidimensional finite elements. *Comput. Methods Appl. Mech. Eng.* 2009; **198**(21-26):1716–1725.
28. Kim K, Yi D, Lee S. Mortar method for nonconforming finite elements. *Appl. Math. Comput.* 2005; **167**(1):650–669.
29. Cockburn B, Shu CW. The local discontinuous Galerkin method for time-dependent convection-diffusion systems. *SIAM J. Numer. Anal.* 1998; **35**(6):2440–2463.
30. Arnold DN, Brezzi F, Cockburn B, Marini LD. Unified analysis of discontinuous Galerkin methods for elliptic problems. *SIAM J. Numer. Anal.* 2001; **39**(5):1749–1779.
31. Peraire J, Persson PO. The compact discontinuous Galerkin (CDG) method for elliptic problems. *SIAM J. Sci. Comput.* 2008; **30**(4):1806–1824.
32. Feng X, Wu H. Discontinuous Galerkin methods for the Helmholtz equation with large wave number. *SIAM J. Sci. Comput.* 2009; **47**(4):2872–2896.
33. Alvarez GB, Loula AFD, do Carmo EGD, Rochinha FA. A discontinuous finite element formulation for Helmholtz equation. *Comput. Methods Appl. Mech. Eng.* 2006; **195**(33-36):4018–4035.
34. Arnold DN. An interior penalty finite element method with discontinuous elements. *SIAM J. Numer. Anal.* 1982; **19**(4):742–760.
35. Cockburn B, Dong B, Guzmán J. A superconvergent LDG-hybridizable Galerkin method for second-order elliptic problems. *Math. Comp.* 2008; **77**(264):1887–1916.
36. Nguyen NC, Peraire J, Cockburn B. An implicit high-order hybridizable discontinuous Galerkin method for linear convection-diffusion equations. *J. Comput. Phys.* 2009; **228**(9):3232–3254.
37. Nguyen N, Peraire J, Cockburn B. A hybridizable discontinuous Galerkin method for Stokes flow. *Comput. Methods Appl. Mech. Eng.* 2010; **199**(9-12):582–597.
38. Cockburn B, Gopalakrishnan J, Lazarov R. Unified hybridization of discontinuous Galerkin, mixed, and continuous Galerkin methods for second order elliptic problems. *SIAM J. Numer. Anal.* 2009; **47**(2):1319–1365.
39. Kirby R, Sherwin S, Cockburn B. To CG or to HDG: A comparative study. *J. Sci. Comput.* 2011; **51**(1):183–212.
40. Berenger JP. A perfectly matched layer for the absorption of electromagnetic waves. *J. Comput. Phys.* 1994; **114**(2):185–200.
41. Singer I, Turkel E. A perfectly matched layer for the Helmholtz equation in a semi-infinite strip. *J. Comput. Phys.* 2004; **201**(2):439–465.
42. Berkhoff JCW. Computation of combined refraction-diffraction. *Proceedings of the 13th Coastal Engineering Conference*, vol. 1, ASCE: Vancouver, Canada, 1972; 471–490.
43. Booij N. A note on the accuracy of the mild-slope equation. *Coast. Eng.* 1983; **7**(3):191–203.
44. Chen H. Effects of bottom friction and boundary absorption on water wave scattering. *Appl. Ocean Res.* 1986; **8**(2):99–104.
45. Zhao L, Panchang V, Chen W, Demirbilek Z, Chhabbra N. Simulation of wave breaking effects in two-dimensional elliptic harbor wave models. *Coast. Eng.* 2001; **42**(4):359–373.
46. Berkhoff J. Mathematical models for simple harmonic linear water waves: wave diffraction and refraction. PhD Thesis, Delft Hydraulics Laboratory, Delft University of Technology, Delft, Netherlands 1976.
47. Montlaur A, Fernández-Méndez S, Huerta A. Discontinuous Galerkin methods for the Stokes equations using divergence-free approximations. *Int. J. Numer. Methods Fluids* 2008; **57**(9):1071–1092.
48. Cockburn B, Guzmán J, Wang H. Superconvergent discontinuous Galerkin methods for second-order elliptic problems. *Math. Comput.* 2009; **78**:1–24.
49. Ainsworth M, Oden JT. *A posteriori error estimation in finite element analysis*. Pure and Applied Mathematics (New York), Wiley-Interscience [John Wiley & Sons]: New York, 2000.
50. Huerta A, Rodriguez-Ferran A, Díez P, Sarrate J. Adaptive finite element strategies based on error assessment. *Int. J. Numer. Methods Eng.* 1999; **46**(10):1803–1818.

51. Díez P, Arroyo M, Huerta A. Adaptivity based on error estimation for viscoplastic softening materials. *Mech. Cohesive-Frict. Mater.* 2000; **5**(2):87–112.
52. Sauer-Budge AM, Bonet J, Huerta A, Peraire J. Computing bounds for linear functionals of exact weak solutions to Poisson's equation. *SIAM J. Numer. Anal.* 2004; **42**(4):1610–1630.
53. Parés N, Bonet J, Huerta A, Peraire J. The computation of bounds for linear-functional outputs of weak solutions to the two-dimensional elasticity equations. *Comput. Methods Appl. Mech. Engrg.* 2006; **195**(4-6):406–429.
54. Parés N, Díez P, Huerta A. Bounds of functional outputs for parabolic problems. II. Bounds of the exact solution. *Comput. Methods Appl. Mech. Eng.* 2008; **197**(19-20):1661–1679.
55. Parés N, Díez P, Huerta A. Exact bounds for linear outputs of the advection-diffusion-reaction equation using flux-free error estimates. *SIAM J. Sci. Comput.* 2009; **31**(4):3064–3089.
56. Díez P, Jose Rodenas J, Zienkiewicz OC. Equilibrated patch recovery error estimates: simple and accurate upper bounds of the error. *Int. J. Numer. Methods Eng.* 2007; **69**(10):2075–2098.
57. Ladevèze P, Pelle JP. *Mastering calculations in linear and nonlinear mechanics*. Mechanical Engineering Series, Springer-Verlag: New York, 2005. Translated from the 2001 French original by Theofanis Strouboulis.
58. Parés N, Díez P, Huerta A. Subdomain-based flux-free a posteriori error estimators. *Comput. Methods Appl. Mech. Engrg.* 2006; **195**(4-6):297–323.
59. Eskilsson C. An hp-adaptive discontinuous Galerkin method for shallow water flows. *Int. J. Numer. Methods Fluids* 2011; **67**(11):1605–1623.
60. Díez P, Huerta A. A unified approach to remeshing strategies for finite element h-adaptivity. *Comput. Methods Appl. Mech. Eng.* 1999; **176**(1-4):215–229.
61. Huerta A, Díez P. Error estimation including pollution assessment for nonlinear finite element analysis. *Comput. Methods Appl. Mech. Eng.* 2000; **181**(1-3):21–41.
62. Remacle JF, Flaherty JE, Shephard MS. An adaptive discontinuous Galerkin technique with an orthogonal basis applied to compressible flow problems. *SIAM Rev.* 2003; **45**(1):53–72.
63. Thompson LL, Pinsky PM. Complex wavenumber Fourier analysis of the p-version finite element method. *Comput. Mech.* 1994; **13**(4):255–275, doi:10.1007/BF00350228.
64. Zienkiewicz O, Taylor R, Nithiarasu P. *The Finite Element Method for Fluid Dynamics*. Sixth edn., Elsevier Butterworth-Heinemann: Jordan Hill, Oxford, 2005.
65. Sarrate J, Roca X, Ruiz-Girones E. EZ4U Mesh generation environment. URL `www.lacan.upc.edu/ez4u.htm`.
66. Higham NJ. *Accuracy and stability of numerical algorithms*. Second edn., Society for Industrial and Applied Mathematics (SIAM): Philadelphia, PA, 2002, doi:10.1137/1.9780898718027.
67. Roca X, Gargallo-Peiró A, Sarrate J. Defining quality measures for high-order planar triangles and curved mesh generation. *Proceedings of the 20th International Meshing Roundtable*, Paris, France, 2011.
68. MacCamy RC, Fuchs RA. Wave forces on piles: a diffraction theorys. *Technical Report*, US Army Corps of Engineering, Beach Erosion Board, Washington, DC 1954.